Journal of Power Sources 192 (2009) 660–667

Contents lists available at ScienceDirect

Journal of Power Sources

journal homepage: www.elsevier.com/locate/jpowsour

Formation mechanism of $LiFePO_4$/C composite powders investigated by X-ray absorption spectroscopy

Kuei-Feng Hsu[a,b], Shao-Kang Hu[a,b], Chinh-Hsiang Chen[a], Ming-Yao Cheng[a], Sun-Yuan Tsay[b], Tse-Chuan Chou[b], Hwo-Shuenn Sheu[c], Jyh-Fu Lee[c], Bing-Joe Hwang[a,c,*]

[a] Department of Chemical Engineering, National Taiwan University of Science & Technology, 43 Keelung Road, Sec. 4, Taipei 106, Taiwan
[b] Department of Chemical Engineering, National Cheng Kung University, No. 1, Ta-Hsueh Road, Tainan 701, Taiwan
[c] National Synchrotron Radiation Research Center, Hsinchu 300, Taiwan

ARTICLE INFO

Article history:
Received 30 December 2008
Received in revised form 19 February 2009
Accepted 24 February 2009
Available online 9 March 2009

Keywords:
Li ion battery
$LiFePO_4$
Mechanism
Cathode
XAS

ABSTRACT

The local structure and oxidation states for both the precursors and the $LiFePO_4$/C composite powders were investigated by X-ray absorption spectroscopy (XAS) to provide a deep insight into their formation mechanism. It was found that the local structure and oxidation states of the precursors and the synthesized $LiFePO_4$/C powders as well as the electrochemical properties of the synthesized powders were strongly influenced by the *R* ratio (*R*: molar ratio of citric acid to total metal ions). The oxidation states of iron ions of the precursors for $R = 1$ and 0.75 consist mainly of Fe(II) and traces of Fe(III). However, the oxidation state of iron ions of the precursor for $R = 0.5$ comprises mainly of Fe(III). The oxidation state of iron ions of all the synthesized powders is Fe(II). The structure of the precursors and the synthesized powders for $R = 1$ and 0.75 is more ordering than that for $R = 0.5$. It is in good agreement with the observation of the cation mixing obtained from the Riteveld analysis of the XRD data. The better the electrochemical performance is, the more ordering the structure or the less the cation mixing. However, the effect of the *R* values on the carbon content is also essential for the electrochemical properties of the synthesized $LiFePO_4$/C composite powders. Increasing the carbon content leads to the increase in the electronic conductivity but impedes the Li^+ ion diffusion of the composite materials. Consequently, the powders synthesized at the optimal *R* ratio of 0.75 exhibited the highest initial capacity, about 150 mAh g^{-1} when cycled at 1/40 C rate at room temperature. The structural scheme of the precursors and the synthesized powders and the formation mechanism of the $LiFePO_4$/C composite powders are also addressed in this work.

1. Introduction

Since the demonstration of electrochemically reversible lithium insertion–extraction for $LiFePO_4$ in 1997 [1], lithium transition metal phosphate with an ordered olivine structure, $LiMPO_4$ (M = Co, Ni, Mn, Fe, Cu) has attracted much attention as promising new cathode materials for rechargeable lithium batteries [2–7]. One of the most promising candidates for rechargeable lithium batteries is $LiFePO_4$. Moreover, lithium can be extracted from $LiFePO_4$ and inserted into $FePO_4$ along with a flat potential plateau at 3.5 V *vs.* Li/Li^+ together with a theoretical specific capacity of 170 mAh g^{-1} [1]. $LiFePO_4$ is inexpensive, nontoxic, nonhygroscopic, and environmentally friendly. It occurs in nature as the mineral triphylite, has an orthorhombic unit cell (space group Pnma). Both Li and Fe atoms are in octahedral sites with Li located in the 4a and Fe in the 4c positions. The O sites form a nearly tetrahedral arrangement about P sites and also form an approximately octahedral arrangement about each Fe site. It is apparent that there are channels along the *b*-axis which accommodate mobile Li^+ ions [8,9]. When Li^+ ions and electrons are removed from $LiFePO_4$, the remaining $FePO_4$ framework has same structure, with a small (7%) reduction in volume [10,11]. The volumetric expansion and the structural charge during Li^+ intercalation are low compared to other intercalation compounds, which is advantageous for the achievement of a high cycle life.

XAS is a powerful technique to probe both electronic structure and local structure of new materials. Information about the valence state of the investigated element and its electron configuration can be obtained from the X-ray absorption near-edge structure (XANES) region, whereas the extended X-ray absorption fine structure (EXAFS) region can provide the local structure of absorbing atom. Recently, some groups have investigated the oxidation state and local structure of the $LiFePO_4$ powders by means of X-ray absorption spectroscopy (XAS) [12–15]. The features in the region of the $1s \rightarrow 3d$ transition have been shown to be very sensitive to the

* Corresponding author at: Department of Chemical Engineering, National Taiwan University of Science & Technology, 43 Keelung Road, Sec. 4, Taipei 106, Taiwan. Tel.: +886 2 27276624.
E-mail address: bjh@mail.ntust.edu.tw (B.-J. Hwang).

0378-7753/$ – see front matter © 2009 Elsevier B.V. All rights reserved.
doi:10.1016/j.jpowsour.2009.02.076

oxidation state and geometry of the iron atom in the XANES region [16]. X-ray absorption spectroscopy has been used to determine the structural variation of Li_xFePO_4 electrode material during cycling. They have reported that Fe ions are octahedrally coordinated and in the Fe^{2+} state. Even after repeated charging and discharging, the structure of the $LiFePO_4$ cycled electrodes did not change. The preparation conditions may change the local structure of precursors and $LiFePO_4$ powders which will affect their electrochemical properties significantly. Unfortunately, no report has studied the oxidation state and local structure of precursors and $LiFePO_4$ powders prepared at various conditions to our knowledge. It is also of great interest to understand the relationship between the structure of synthesized powders and their corresponding precursors.

The $LiFePO_4$/carbon composite cathode materials were successfully synthesized by our developed sol–gel process [17,18], which is not only easy but also low cost. The much cheaper precursor, iron powder instead of iron salt was employed in our developed process. The citric acid in the developed process plays the role not only as a complexing agent but also as a carbon source, which improves the conductivity of the composites and hinders the growth of $LiFePO_4$ particles. The nano-sized $LiFePO_4$ particles without the impurity phase have been successfully synthesized.

It is of great importance for the further improvement of the performance of $LiFePO_4$ powders to investigate its formation mechanism in our developed process. Meanwhile, it is also interesting to study the role of the molar ratio of citric acid to total metal ions (R) in the process. This work provides a deep insight into the formation mechanism based on the local structure and oxidation states of not only the precursors but also the $LiFePO_4$/C composite powders which are prepared at various R values are investigated by employing X-ray absorption spectroscopy (XAS). The effects of the R values on the local structure and electrochemical properties of $LiFePO_4$/C are also discussed.

2. Experimental

2.1. Synthesis

A sol–gel route using iron powders as starting materials was employed to obtain the $LiFePO_4$ cathode materials. The detailed procedures used in this work for the sol–gel preparation of the materials have been described in our previous papers [17–19]. $LiFePO_4$ samples were synthesized by a sol–gel method using citric acid as a chelating agent [17,18]. Stoichiometric amounts of iron powder and lithium nitrate were dissolved into an aqueous solution of saturated citric acid with continuous stirring. Then 10 ml of a saturated aqueous solution of ammonium dihydrogen phosphate was added. The mixtures were heated gently with continuous stirring for 4 h to remove excess water. The resulting gel precursor was dried in a circulation oven for a week at 60 °C. The precursors were further calcined at 850 °C in 99.999% nitrogen atmosphere for 2 h. The heating rate of the furnace was 10 °C min^{-1}. The precursors and the calcined powders were prepared at various molar ratios of citric acid to total metal ions (R) of 1, 0.75, and 0.5 for the further XAS investigation.

2.2. Characterization

2.2.1. Carbon content

To determine the carbon content, elemental analysis was performed (EA, Heraeus CHN-O Rapid Analyzer) for the powders prepared at various R values.

2.2.2. XRD

X-ray diffraction patterns of the synthesized powders were collected for structural analysis. The XRD data were obtained over an angular 2θ range from 10° to 60° with a step size of 0.01° and a constant counting time of 5 s per step using a powder X-ray diffractometer (Cu K_α radiation). X-ray Rietveld refinements were performed using the GSAS (General Structure Analysis System) program to obtain the crystal structure parameters [20].

2.2.3. X-ray absorption spectroscopy measurement

X-ray absorption spectra (XAS) have been recorded at the beam line BL17C of National Synchrotron Radiation Research Center (NSRRC) at Hsinchu, Taiwan. The storage ring was operated with electron energy of 1.5 GeV and a current between 100 and 200 mA. Data collection was carried out in the transmission mode with a Si(1 1 1) double crystal monochromator. High order harmonics was eliminated by adjusting the parallelism of the monochromator crystals. The intensities of incident and transmitted beams were monitored using ionization chambers as detectors. The edge jump of the samples was properly adjusted to improve the S/N ratio of spectra. The measurement for energy calibration was performed in each scan using the Fe foil as a reference which was positioned in front of the window of the third ionization chamber. During XAS measurements, the beam size was limited by the horizontal and vertical slits with the area of 2 mm × 2 mm.

2.2.4. EXAFS data analysis

Standard procedures were followed to analyze the EXAFS data. First, the raw data undergo background subtraction and normalized. The normalized EXAFS data ($\chi(E)$) was Fourier transformed from energy space to k-space, where k is the photoelectron wave vector. The $\chi(k)$ data described the oscillation of the backscattering wave through the local environment of about ~10 Å, which give us the surrounding information for the central atom. For the $LiFePO_4$ material, the k^3-weighted EXAFS spectra, $k^3\,\chi(k)$, for the selected absorber Fe, were calculated to compensate the damping of the EXAFS oscillations in high-k region. Subsequently, k^3-weighted $\chi(k)$ data in the k-space ranging from 3.8 to 10.6 $Å^{-1}$ for Fe K-edge, respectively, was Fourier transformed (FT) to r-space in order to separate the EXAFS contributions from different coordination shells. A nonlinear least-squares algorithm was applied for curve fitting of EXAFS in r-space between 0.8 and 4.2 Å for Fe K-edge, respectively.

The structure parameters such as coordination numbers (N), bond distances (R) and Debye–Waller factor were extracted by curve fitting analysis based on Winxas 2.3. The theoretical EXAFS parameters, the backscattering amplitude and the phase shift, were calculated by FEFF7 code [21] for all possible scattering paths which were generated from the crystallographic model of the known structures. The amplitude reduction factor S_0^2 was scaled to a fixed value of 0.72 after preliminary refinements. The structure parameters describing the local environment for $Li_{1-x}FePO_4$ were obtained from the EXAFS data with Winxas 2.3 and the FEFF7 code. In all cases, the values of Residual factor defined by the following equation are less than 10, indicating that the fitting error is quite small.

$$\text{Residual factor}\,(\%) = \frac{\sum_{i=1}^{N} |y_{\text{exp}}(i) - y_{\text{theo}}(i)|}{\sum_{i=1}^{N} |y_{\text{exp}}(i)|} \times 100$$

where y_{exp} and y_{theo} are experimental and theoretical data points, respectively.

2.2.5. Electrochemical properties

Electrochemical characterization was carried out with coin-type cells. The electrode was prepared by using 83% of $LiFePO_4$/carbon active material, 11% Super P carbon black, and 6% polyvinylidene difluoride (PVdF), as binder, dissolved in N-methyl-2-pyrrolidinone (NMP) solvent. The obtained slurry was then cast on an Al current collector and dried for 2 h in an oven at 100 °C. The resulting elec-

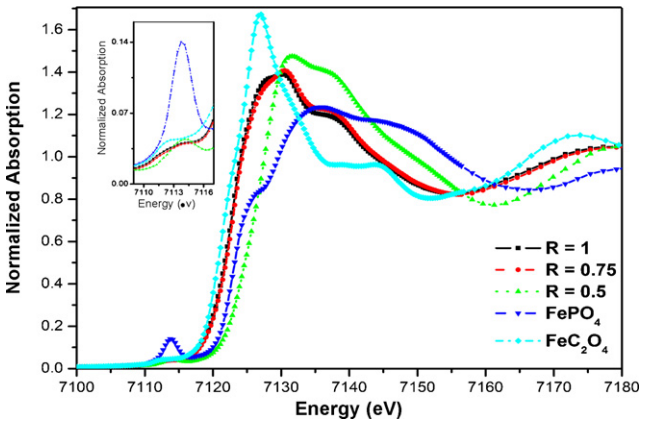

Fig. 1. Normalized absorption of Fe K-edge for $LiFePO_4$ precursors at various R values, along with the references of $FePO_4$ and FeC_2O_4.

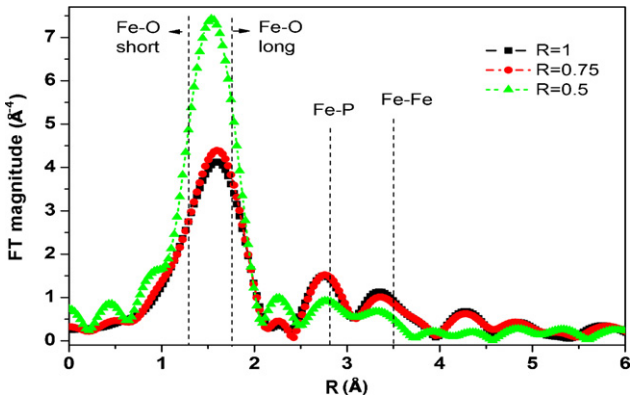

Fig. 2. k^3-Weighted FT spectra of Fe K-edge for $LiFePO_4$ precursors at various R values.

trode film was subsequently pressed and punched into a circular disc. The electrode films are preserved in an argon-filled glove box (Unilab, Mbruan). The coin cell was fabricated using lithium metal as a counter electrode. The electrolyte used consisted of a 1 M solution of $LiPF_6$ in a mixture 1:1 by volume of ethylene carbonate (EC) and diethyl carbonate (DEC). The separator (Celgard 2400, Hoechst Celenese Corp.) was soaked in an electrolyte for 24 h prior to use. All the weighing procedure and coin cell assembly were performed in an argon-filled glove box by keeping both oxygen and moisture level less than 1 ppm. The charge–discharge measurements were performed on the coin cells using a programmable battery tester (Maccor 2300) at different C-rates over a potential range of 3.0–4.0 V.

3. Results and discussion

3.1. XANES of the precursors

Here the pre-edge peak of X-ray absorption spectroscopy is the most useful feature to determine the oxidation state and symmetry of Fe sites. The Fe K-edge XANES spectra of the $LiFePO_4$ precursors prepared at various R values and the references of $FePO_4$ as well as FeC_2O_4 are shown in Fig. 1. According to the literature [16,22], the Fe pre-edge peak around 7112 eV corresponds to the $1s \rightarrow 3d$ transition, which is a dipole forbidden process for the Fe site of $LiFePO_4$. A weak absorption peak at this energy is due to the hybridization of Fe 3d orbital with O 4p orbital (3d–4p mixing). It is sufficient to determine the oxidation state of Fe from its pre-edge feature [22]. Fig. 1 shows the peak energy for the precursors of $R = 1$ and 0.75 is similar and close to that of FeC_2O_4, indicating that their iron oxidation state consist mainly of Fe(II) and traces of Fe(III). However, the higher peak energy (~7114 eV) of the precursor of $R = 0.5$, indicating its iron oxidation state comprises mainly of Fe(III).

3.2. EXAFS of the precursors

Fig. 2 shows the radial structure functions obtained from Fourier transformation (FT) of the $k^3\chi(k)$ functions in the k-space range between 3.8 and 10.6 $Å^{-1}$ for the precursors at various R values. The radial structure function indicates the scattering contribution of different atomic shells around the X-ray absorbing iron atoms. The first strong peak corresponds to the scattering process of the ejected electron at the oxygen-containing coordination shell, and the second and the third peaks are contributed from the scattering process of the ejected electron at the phosphorous- and iron-containing coordination shells, respectively. The features of the peaks contributed from the Fe–O, Fe–P, and Fe–Fe shells are almost identical for the precursors of $R = 1$ and 0.75, implying that the local environment of Fe in the both samples are nearly the same. It is suggested that the formation reactions of the precursors are alike during the sol–gel process for $R = 1$ and 0.75. For $R = 0.5$, the features of the first three peaks change considerably. The FT corresponding to Fe–O shell for $R = 0.5$ is much higher than that of $R = 1$ and 0.75, indicating that the local environment around the iron ion is changed dramatically for the precursor of $R = 0.5$. It implies that the iron environment for the precursor of $R = 0.5$ might be completely different from that for the precursor of $R = 1$ and 0.75.

The coordination atom of the first and the second shells are considered to be oxygen, and that of the third and the fourth shells are considered to be phosphorous and iron, respectively in the fitting model. The structural parameters of the $LiFePO_4$ precursors shown in Table 1 are obtained from the FEFF-fit analysis of their corresponding $k^3\chi(k)$ functions using possible scattering paths in the

Table 1
Structural parameters of Fe K-edge for $LiFePO_4$ precursors at various R values simulated by four-shell model.

R value	Sphere	Shell	Coordination number (N)	Radius R_j (Å)	Debye–Waller factor σ_j^2 ($\times 10^{-3}$ Å^2)	Residual %
1	1st	Fe–O1	3	1.91	10.7	3.53
	2nd	Fe–O2	3	2.09	6.6	
	3rd	Fe–P	1	3.15	2.9	
	4th	Fe–Fe	1	3.75	8.5	
0.75	1st	Fe–O1	3	1.92	11.3	2.35
	2nd	Fe–O2	3	2.08	6.2	
	3rd	Fe–P	1	3.16	5.0	
	4th	Fe–Fe	1	3.73	8.8	
0.5	1st	Fe–O1	4	1.92	8.0	3.69
	2nd	Fe–O2	4	2.03	5.6	
	3rd	Fe–P	1	3.18	4.4	
	4th	Fe–Fe	0	0.00	0.0	

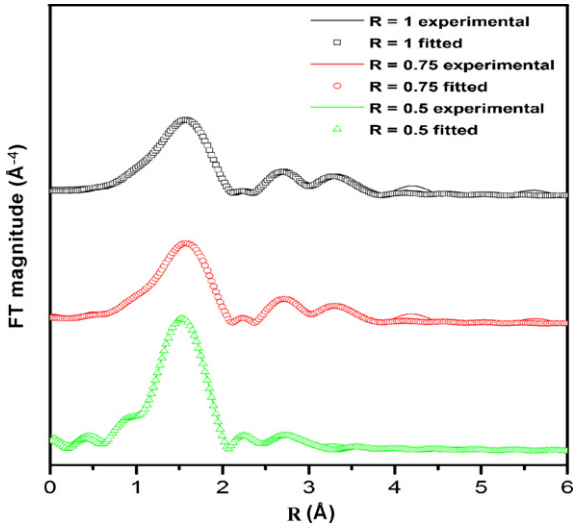

Fig. 3. FEFF7 fit the radial structure function for $LiFePO_4$ precursors.

model. The experimental Fourier-filtered curve matches very well with the simulated one for the $LiFePO_4$ precursor at various R values, as shown in Fig. 3. It implies that the proposed model is suitable to describe the structure of the precursor.

According to the Pourbaix diagram for iron [23], iron powder would be oxidized to Fe^{2+} while hydrogen ions are being reduced to hydrogen in the citric acid solution in which pH is about 2. The generated Fe^{2+} ions will be chelated by citric acid immediately and form a stable complex (Cit^{3-}–Fe^{2+}) if the R value is high enough. However, if the R value is too low, the generated Fe^{2+} ions will be further oxidized to the ferric ions associated with the reduction reaction of the dissolved oxygen and then a Cit^{3-}–Fe^{3+} complex formed instead of a Cit^{3-}–Fe^{2+} one. This formation process of the precursor is depicted in Fig. 4.

According to Table 1, the Fe–O1, F–O2, Fe–P and Fe–Fe distances are 1.91, 2.09, 3.15 and 3.75 Å, respectively and their corresponding coordination numbers are 3, 3, 1 and 1, respectively, for the precursor of $R = 1$. It indicates that the iron site is octahedrally coordinated by 6 oxygen ions. However, the octahedral coordination is distorted with 3 short Fe–O1 and 3 long Fe–O2 bonds. There is one P and one Fe in the third and fourth shells, respectively. The structural parameters and the coordination number (N) for the precursor of $R = 1$ and 0.75 are almost identical, as shown in Table 1, indicating their local structure is similar. However, the magnitude of the FT peak corresponding to the Fe–O shell becomes larger for the precursor of $R = 0.5$ compared to $R = 1.0$ and 0.75. The coordination number of the Fe–O1, Fe–O2, Fe–P and Fe–Fe for the precursor of $R = 0.5$ are 4, 4, 1 and 0, respectively, indicating the coordination number of

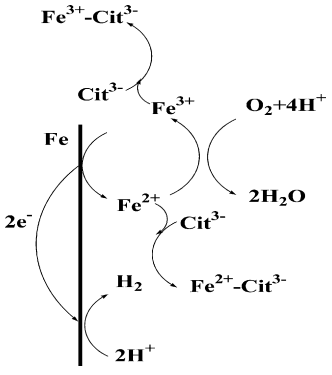

Fig. 4. Schematic representation of the formation process.

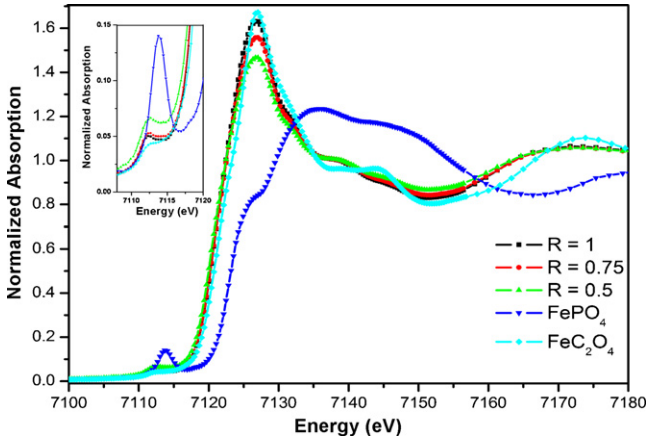

Fig. 5. Normalized absorption of Fe K-edge for $LiFePO_4$/C composite powders at various R values, along with the references of $FePO_4$ and FeC_2O_4.

the Fe–O increases but the coordination of the Fe–Fe disappears. The Fe atoms for the precursor of $R = 1$ and 0.75 are surrounded by six oxygen ions but by eight oxygen ions for the precursor of $R = 0.5$. Although a iron complex with 8-coordinate geometry is rare, the square antiprism and dodecahedron are common in transition metal complexes, and there are some 8-coordinate iron complexes such as almandine-rich garnet $[Fe(EDTA)(H_2O)_2]^+$ etc. [24,25]. It is suggested that the iron ion in the precursor for $R = 0.5$ must have more space to accommodate eight ligands than in the other samples. Meanwhile, the distortion in the precursor of $R = 0.5$ is more serious than that in the precursor of $R = 1.0$ and 0.75.

3.3. XANES of the synthesized powders

As shown in Fig. 5, the peak in the pre-edge region represents an s–d like transition which is originally dipole forbidden, but it becomes partially allowed by mixing of the d-states of the transition metal with the p-states of the surrounding oxygen atoms. Its energy position depends mainly on the Fe oxidation state, whereas its intensity depends on the geometry around [22,25–27], so that it will be virtually zero in case of regular octahedral symmetry (O_h) around the absorber, and it will reach its maximum in case of tetrahedral coordination (T_d). The XANES of the $LiFePO_4$ powders prepared at various R values is shown in Fig. 5. To facilitate comparison, the pre-edge region of the corresponding spectra here has been magnified in Fig. 5. The pre-edge bands of iron(II) and iron(III) complexes have been extensively investigated in the literature [22,25]. Meanwhile, the pre-edge bands of $LiFePO_4$ and $FePO_4$ were also well-discussed [14]. A full explanation of the pre-edge features is beyond the aim of the present work. Briefly, the occurrence of this peak is related to the nature of $1s \rightarrow 3d$ transition, which is electric dipole forbidden but quadrupole allowed. The pre-edge intensity is the most sensitive to site centrosymmetry with the most centrosymmetric Fe coordination having the lowest intensity. From the observation of Fig. 5 it reveals that Fe is octahedrally coordinated by oxygen in the $LiFePO_4$ powders. The reference $FePO_4$ (purchased from Merck) has a trigonal structure with a space group of P_{13121}. The symmetry of the iron site in the reference $FePO_4$ is tetrahedral, which is different from an octahedral site in the fully charged sample reported in the literature [14]. The pre-edge region is assigned to be $1s \rightarrow 3d$ transition, and weak intensity in this region indicates an octahedral coordination as opposed to the tetrahedral coordination from which a strong pre-edge intensity ($FePO_4$) is found. Another interesting feature of the XANES spectra shown in Fig. 5 is the 1s–3d pre-edge peak observed for all three $LiFePO_4$-based samples for Fe(II) is at 7112.4 eV which is at lower energies than that for

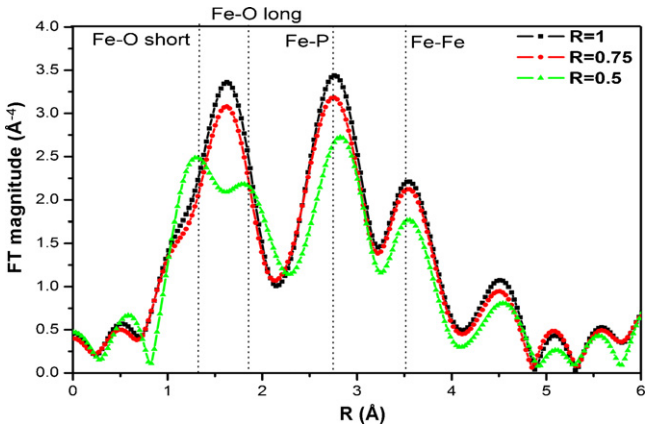

Fig. 6. k^3-Weighted FT spectra of Fe K-edge for $LiFePO_4$/C composite powders at various R values.

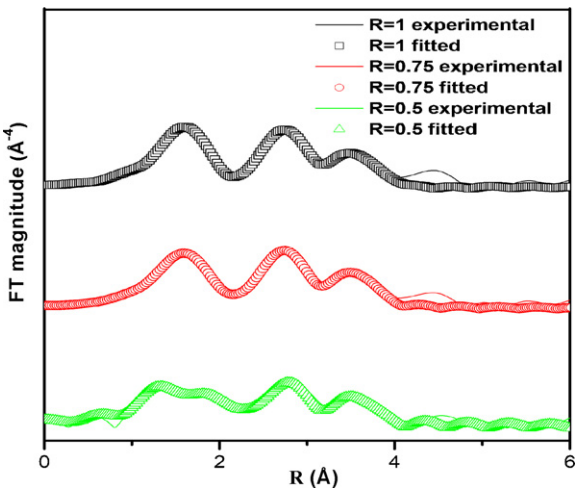

Fig. 7. FEFF7 fit the radial structure function for $LiFePO_4$/C composite powders.

Fe(III) in $FePO_4$ where the pre-edge peak is at 7113.8 eV, indicating the oxidation state of Fe in the synthesized $LiFePO_4$ powders is +2.

The local structure and oxidation state of the precursors and the synthesized $LiFePO_4$/C composite powders were investigated by X-ray absorption spectroscopy (XAS) to provide deep insights into their formation mechanism. Although Fe^{3+} ions exist for the precursor of $R = 0.5$, the oxidation state of iron in all the synthesized powders is +2. It implies that the iron ions would be completely reduced to ferrous ions even the precursor consisting of Fe^{3+} in the developed process.

3.4. EXAFS of the synthesized powders

The Fourier transform (FT) of the Fe K-edge EXAFS spectra for the $LiFePO_4$ powders is shown in Fig. 6. The first strong peak is ascribed to the scattering process of the ejected electron at the oxygen-containing coordination shell, and the second and the third peaks represent the scattering process of the ejected electron at the phosphorous- and iron-containing coordination shells, respectively. For the synthesized powders with $R = 1$ and 0.75, the shape and intensity of the Fe–O, Fe–P, and Fe–Fe peaks are almost same, implying that the local environment of the iron in these two samples is identical. For $R = 0.5$, the feature of the oxygen coordination shell is unlike with that of the other two samples. The splitting of the first peak was observed, indicating that the Fe environment for the powder of $R = 0.5$ is different from that of the other two samples. The shape of peak strongly depends on each sample due to either the crystallographic symmetry or the disordering environment of iron environments.

In the four-shell model, the coordination atom of the first and the second shells are oxygen, and that of the third and the fourth shells are phosphorous and iron, respectively. The experimental Fourier-filtered and simulated data are fitted very well for the synthesized $LiFePO_4$ powders with various R values, as shown in Fig. 7. The structural parameters were obtained by the fitting the EXAFS data with the four-shell model considering possible scattering paths, as shown in Table 2.

It was found that the structural parameters for the $LiFePO_4$ powders of $R = 1$ and 0.75 are similar, as shown in Table 2. However, the coordination number of Fe–Fe and Fe–P shells for the powder of $R = 0.5$ are decreased to be 3 and 4, respectively. It indicates that the local environment of Fe sites in the powders of $R = 1.0$ and 0.75 is different from that in the powders of $R = 0.5$. Considering first the evolution of the Fe–O, Fe–P, and Fe–Fe coordination number, in a perfect $LiFePO_4$ crystal, the Fe atoms are surrounded by six O, five P, and four Fe atoms [28]. It implies that the structure of the $LiFePO_4$ powders of $R = 1$ and 0.75 is more ordering than that of the powder of $R = 0.5$. Based on our experimental observations it is suggested that the $LiFePO_4$ powder with better structural ordering can be achieved from the precursor with better structural ordering. On the contrary, the disordered powders would be obtained if the structure of their corresponding precursor is distorted.

3.5. XRD of the synthesized powders

The X-ray diffraction patterns recorded for the synthesized powders with various R values are shown in Fig. 8. Single-phase structure of $LiFePO_4$ was observed for all the samples. No impurity of Fe_2O_3 or Fe_3O_4 can be identified in Fig. 8, implying that Fe(III) does not exist in the synthesized powders. It is consistent

Table 2
Structural parameters of Fe K-edge for $LiFePO_4$/C composite powders at various R values simulated by four-shell model.

R value	Sphere	Shell	Coordination number (N)	Radius R_j (Å)	Debye–Waller factor σ_j^2 ($\times 10^{-3}$ Å^2)	Residual %
1	1st	Fe–O1	4	2.06	7.8	6.52
	2nd	Fe–O2	2	2.33	9.0	
	3rd	Fe–P	5	3.25	4.9	
	4th	Fe–Fe	4	3.94	9.6	
0.75	1st	Fe–O1	4	2.03	8.2	4.85
	2nd	Fe–O2	2	2.28	10.3	
	3rd	Fe–P	5	3.23	5.1	
	4th	Fe–Fe	4	3.92	9.4	
0.5	1st	Fe–O1	3	1.98	1.6	9.88
	2nd	Fe–O2	3	2.16	0.0	
	3rd	Fe–P	4	3.21	5.5	
	4th	Fe–Fe	3	3.94	8.2	

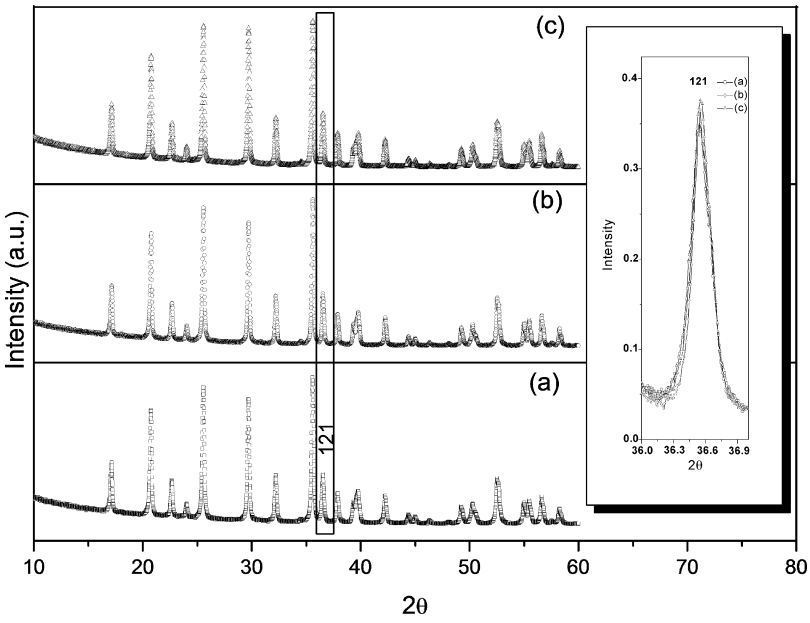

Fig. 8. XRD pattern for $LiFePO_4$/C composite powders prepared at different R ratios: (a) $R = 1$, (b) $R = 0.75$, (c) $R = 0.5$.

with the observation from the XANES feature of the synthesized powders. Since the carbon is formed during the pyrolysis of citric acid, the Fe(III) in the precursor can be completely reduced to Fe(II) by the oxidation of the formed carbon and the formed Fe(II) ions further react with lithium and phosphate ions to form $LiFePO_4$ powder [17,18]. The grain size (t) is calculated from XRD patterns using the Scherrer formula $t = 0.9\lambda/(B\cos\theta)$, where λ is the wavelength of the X-ray used, B the width at an intensity equal to half of I_{max}, and θ the Bragg angle of the diffraction peak considered. The grain size is found to be 42, 44, and 47 nm for $R = 1$, 0.75, and 0.5, respectively. The grain size of the $LiFePO_4$ is increased insignificantly with R value in the developed process. It is obviously observed that the growth of the $LiFePO_4$ grains is inhibited by the formed carbons. This phenomenon is in good agreement with our previous report [17,18], indicating that the nano-sized $LiFePO_4$ and its derivatives can be obtained by the developed sol–gel process.

The XRD data have been normalized with respect to the intensity of (3 1 1) peak, as shown in Fig. 8. The normalized intensity of (1 2 1) is increased with a decrease in the R values. Since the structure factor of (1 2 1) plane is only contributed from lithium and oxygen ions, partial interchange of occupancy of the Li^+ ions and Fe^{2+} ions among the sites will lead to increase in the $I(1\,2\,1)/I(3\,1\,1)$ peak ratio. Therefore, the normalized intensity will increase if the cation mixing between Li^+ and Fe^{2+} increases. It indicates that the cation mixing of the obtained powders decreases with an increase in the R values. Further study on the structural characterization of the olivine was undertaken by Rietveld refinement of the XRD data, using the GSAS software suite. The structural model and parameters for olivine $LiFePO_4$ proposed by Streltsov [28] were utilized as the starting attempt. Fig. 9 shows the result of fitting and the difference between the observed and calculated data. The observed and calculated patterns match very well. The final structural parameters for all the samples are collected in Table 3. The reliability factors (R_{wp}) for all the samples were quite good, i.e., around 6%. It was found that the lattice parameters of the synthesized $LiFePO_4$ are influenced by the R values. Decreasing the R values leads to expand the a-, b- and c-axes, as well as increase the orthorhombic unit cell volume from 290.03 to 291.92 $Å^3$. Cho et al. [29] have suggested that the lattice parameters increase if the iron ion is reduced from Fe^{3+} (0.64 Å) to Fe^{2+} (0.77 Å) in their synthesized powders. However, there is no change in the valence state of the iron ions in their samples from their Fe K-edge XANES. The variation of the lattice parameters is probably from the other reason. We suggest that the unit cell volume will increase if partial cation mixing occurs even there is no change in the valence state of iron ions. It is consistent with the data reported by Yang et al. [30–32]. The reason is the ionic radius of divalent iron (Fe^{2+}, 0.77 Å) is somewhat larger than that of lithium ion (Li^+, 0.68 Å). Therefore, the lattice parameters will increase if the Li^+ and Fe^{2+} ions occupy 4c and 4a sites, respectively. The simulation model proposed by Isiam et al. [33] shows that the most favorable intrinsic defect is the Li–Fe "anti-site" pair in which a Li^+ (on the M1 site) and an Fe^{2+} (on the M2 site) are interchanged. As the R value is increased from 0.5 to 1, the cation mixing ratio decrease from 6.4 to 2.8%. It demonstrates the molar ratio of citric acid to metal ions plays an important role in the synthesis process. The R value is therefore a sensitive indicator of a change in local environment or a local distortion around the central atom.

3.6. Electrochemical properties

The cycling behaviors of the $LiFePO_4$/carbon cells were tested at a C-rate of 1/40 between 3.0 and 4.0 V. The cycle-life plots of $R = 1$, 0.75 and 0.5 are shown in Fig. 10. The first discharge spe-

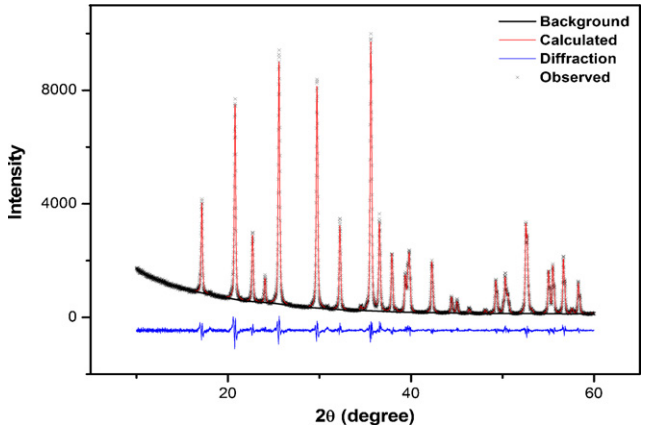

Fig. 9. Results of fitting the X-ray powder diffraction data corresponding to olivine $LiFePO_4$ for $LiFePO_4$/C composite powders ($R = 1$).

Table 3
Structural parameters obtained from Rietveld refinement of olivine type orthorhombic $LiFePO_4$/C composite calcined at 850 °C for 2 h with various R value (space group = Pnma (62)).

Atom	Site	Symm	x/a	y/b	z/c	Occ.	U_{iso}(Å^2)
R = 1 (R_p = 4.40%, R_{wp} = 5.81%, χ^2 = 2.94,R_F^2 = 2.29%, a = 10.3161, b = 5.9993, c = 4.6863)							
Li	4a	−1	0	0	0	0.9779	0.0896(5)
Fe	4a	−1	0	0	0	0.0281	0.0896(5)
Fe	4c	.m.	0.2821(9)	1/4	0.9745(8)	0.9779	0.0040(5)
Li	4c	.m.	0.2821(9)	1/4	0.9745(8)	0.0281	0.0040(5)
P	4c	.m.	0.0946(7)	1/4	0.4157(7)	1	0.0023(4)
O(1)	4c	.m.	0.0975(2)	1/4	0.7426(5)	1	0.0002(1)
O(2)	4c	.m.	0.4575(9)	1/4	0.2057(8)	1	0.008(0)
O(3)	8d	1	0.1676(3)	0.0430(8)	0.2833(3)	1	0.0026(3)
R = 0.75 (R_p = 4.48%, R_{wp} = 6.07%, χ^2 = 2.82, R_F^2 = 2.24%, a = 10.3322, b = 6.0085, c = 4.6933)							
Li	4a	−1	0	0	0	0.9522	0.0130(0)
Fe	4a	−1	0	0	0	0.0478	0.0130(0)
Fe	4c	.m.	0.2823(4)	1/4	0.9745(8)	0.9522	0.0001(6)
Li	4c	.m.	0.2823(4)	1/4	0.9745(8)	0.0478	0.0001(6)
P	4c	.m.	0.0948(3)	1/4	0.4171(1)	1	0.0013(8)
O(1)	4c	.m.	0.0975(6)	1/4	0.7494(9)	1	0.0020(0)
O(2)	4c	.m.	0.4540(7)	1/4	0.2033(6)	1	0.0058(0)
O(3)	8d	1	0.1668(6)	0.0424(3)	0.2820(6)	1	0.0127(2)
R = 0.5 (R_p = 4.57%, R_{wp} = 6.09%, χ^2 = 3.231, R_F^2 = 2.02%, a = 10.3383, b = 6.0122, c = 4.6965)							
Li	4a	−1	0	0	0	0.9359	0.0716(7)
Fe	4a	−1	0	0	0	0.0641	0.0716(7)
Fe	4c	.m.	0.2820(7)	1/4	0.9745(1)	0.9359	0.0054(2)
Li	4c	.m.	0.2820(7)	1/4	0.9745(1)	0.0641	0.0054(2)
P	4c	.m.	0.0946(2)	1/4	0.4131(0)	1	0.0141(8)
O(1)	4c	.m.	0.0965(4)	1/4	0.7426(5)	1	0.0150(6)
O(2)	4c	.m.	0.4517(1)	1/4	0.2082(6)	1	0.0171(7)
O(3)	8d	1	0.1660(7)	0.0401(7)	0.2803(5)	1	0.0109(0)

cific capacity of the R = 1, 0.75 and 0.5 are 118, 152 and 91 mAh g^{-1}, respectively, and after 10 cycles, the discharge specific capacity are 60, 143 and 31 mAh g^{-1}, respectively. The iron ions occupying at lithium sites essentially block the diffusion path of the lithium ions, as the diffusion is fast only along the tunnel and not between them [8]. The more cation mixing ratio is, the higher energy barrier for lithium diffusion. Although increasing the R values leads to improve the structural ordering or avoid the cation mixing between Li^{2+} and Fe^{2+}, the $LiFePO_4$/C composite powders synthesized at R = 0.75 shows the best initial capacity and capacity retention among the synthesized powders. It implies that there are other factors needed to be considered. In addition to the structural ordering, the carbon content in the $LiFePO_4$/C composite powders also plays an important role on their electrochemical performance from our previous studies [17,18]. The carbon contents for the powders synthesized at the R values of 1, 0.75 and 0.5 are 10, 8, and 5 wt%, respectively, as determined using element analysis (EA). The more the carbon content is, the better the electronic conductivity of the $LiFePO_4$/C composite powders. Nazar et al. [34] and Ravet et al. [35] reported the uniform carbon coating can improve the electrochemical performance for $LiFePO_4$. However, the excess residual carbon agglomerating between the composite particles would result in a barrier for lithium ion diffusion [36]. It was suggested that the carbon content in the synthesized powder for R = 1.0 is too much as a result of high energy barrier for lithium ion diffusion and deterioration of its electrochemical properties. Consequently, the electrochemical performance of the synthesized $LiFePO_4$/C composite powders strongly depends on both their carbon content and structural ordering [37].

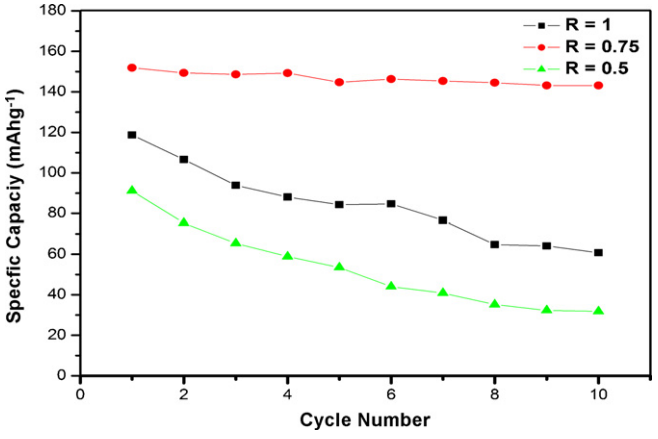

Fig. 10. Dependence discharge capacity against cycle number at 1/40 C rate for the powders synthesized at different R values (R = 1, 0.75 and 0.5).

4. Conclusion

The formation mechanism of the $LiFePO_4$/C composite powders prepared by the developed sol–gel process has been investigated in this study. In the formation mechanism of the precursors, iron powder would be oxidized to Fe^{2+} while hydrogen ions are being reduced to hydrogen in the citric acid solution. The generated Fe^{2+} ions might be chelated with citric ligands immediately and form a stable complex (Cit^{3-}–Fe^{2+}) if the R value is high enough. However, if the R value is too low, the generated Fe^{2+} ions will be further oxidized to the ferric ions associated with the reduction reaction of the dissolved oxygen and then a Cit^{3-}–Fe^{3+} complex formed instead of a Cit^{3-}–Fe^{2+} one. The higher the R value, the better the structural ordering of the precursors. Furthermore, it was found that the synthesized $LiFePO_4$ powder with better structural ordering can be achieved from the precursor with less distortion. It was suggested that the better electrochemical performance can be obtained for the powders with less cation mixing. The effect of the R values on the carbon content is also essential for the electrochemical properties of the synthesized $LiFePO_4$/C composite powders. Increasing the carbon content leads to increase the electronic conductivity but impede the Li^+ ion diffusion path of the composite materials. In addition to the cation mixing, a compromise between electronic conductivity and barrier of lithium ion diffusion needs to be also

considered. Consequently, the $LiFePO_4$/C composite powder synthesized at the optimal *R* value of 0.75 shows the best initial capacity and capacity retention among the synthesized powders.

Acknowledgements

The financial support from the National Science Council of Taiwan, facilities from the National Synchrotron Radiation Research Center (NSRRC), National Cheng-Kung University and the National Taiwan University of Science and Technology are gratefully acknowledged.

References

[1] A.K. Padhi, K.S. Nanjundaswamy, J.B. Goodenough, J. Electrochem. Soc. 144 (1997) 1188.
[2] Y.-N. Xu, W.Y. Ching, Y.-M. Chiang, J. Appl. Phys. 95 (2004) 6583.
[3] N.N. Bramnik, K.G. Bramnik, T. Buhrmester, C. Baehtz, H. Ehrenberg, H. Fuess, J. Solid State Electrochem. 8 (2004) 558.
[4] K. Amine, H. Yasuda, M. Yamachi, Electrochem. Solid-State Lett. 3 (2000) 178.
[5] A.S. Andersson, J.O. Thomas, B. Kalska, L. Häggström, Electrochem. Solid-State Lett. 3 (2000) 66.
[6] A. Yamada, S.C. Chung, J. Electrochem. Soc. 148 (2001) A960.
[7] A. Yamada, S.C. Chung, K. Hinokum, J. Electrochem. Soc. 148 (2001) A224.
[8] D. Morgan, A. Van der Ven, G. Ceder, Electrochem. Solid-State Lett. 7 (2004) A30.
[9] C.Y. Ouyang, S.Q. Shi, Z.X. Wang, X.J. Huang, L.Q. Chen, Phys. Rev. B 69 (2004) 104303.
[10] P. Tang, N.A.W. Holzwarth, Phys. Rev. B 68 (2003) 165107.
[11] A.S. Andersson, J.O. Thomas, J. Power Sources 97–98 (2001) 498.
[12] A. Deb, U. Bergmann, S.P. Cramer, E.J. Cairns, Electrochim. Acta 50 (2005) 5200.
[13] A. Deb, U. Bergmann, E.J. Cairns, S.P. Cramer, J. Synchrotron Radiat. 11 (2004) 497.
[14] A. Deb, U. Bergmann, E.J. Cairns, S.P. Cramer, J. Phys. Chem. B 108 (2004) 7046.
[15] O. Haas, A. Deb, E.J. Cairns, A. Wokaun, J. Electrochem. Soc. 152 (2005) A191.
[16] A.L. Roe, D.J. Schneider, R.J. Mayer, J.W. Pyrz, J. Widom, L. Que, J. Am. Chem. Soc. 106 (1984) 1676.
[17] K.F. Hsu, S.Y. Tsay, B.J. Hwang, J. Power Sources 146 (2005) 529.
[18] K.F. Hsu, S.Y. Tsay, B.J. Hwang, J. Mater. Chem. 14 (2004) 2690.
[19] B.J. Hwang, R. Santhanam, D.G. Liu, Y.W. Tsai, J. Power Sources 102 (2001) 326.
[20] A.C. Larson, R.B. von Dreele, General Structure Analysis System, Los Alamos National Laboratory, Los Alamos, NM, 1994.
[21] S.I. Zabinsky, J.J. Rehr, A. Ankudinov, M.J. Eller, Phys. Rev. B 52 (1995) 2995.
[22] T.E. Westre, P. Kennepohl, J.G. DeWitt, B. Hedman, K.O. Hodgson, E.I. Solomon, J. Am. Chem. Soc. 119 (1997) 6297.
[23] D.A. Jones, Principle and Prevention of Corrosion, 2nd ed., Prentic-Hall, Inc., USA, 1992.
[24] G.L. Miessler, D.A. Tarr, Inorganic Chemistry, 2nd ed., Prentice-Hall Inc., NJ, USA, 1999.
[25] M. Wilke, F. Farges, P.-E. Pett, G.E. Brown Jr., F. Martin, Am. Mineral. 86 (2001) 714.
[26] G. Calas, J. Petiau, Solid State Commun. 48 (1983) 625.
[27] J. Herrero-Martín, J. García, G. Subías, J. Blasco, M.C. Sánchez, J. Phys.: Condens. Matter 16 (2004) 6877.
[28] V.A. Streltsov, E.L. Belokoneva, V.G. Tsirelson, N.K. Hansen, Acta Crystallogr. B49 (1993) 147.
[29] T.H. Cho, H.T. Chung, J. Power Sources 133 (2004) 272.
[30] S. Yang, P.Y. Zavalij, M.S. Whittingham, Electrochem. Commun. 3 (2001) 505.
[31] S. Yang, Y. Song, P.Y. Zavalij, M.S. Whittingham, Electrochem. Commun. 4 (2002) 239.
[32] S. Yang, Y. Song, K. Ngala, P.Y. Zavalij, M.S. Whittingham, J. Power Sources 119–121 (2003) 239.
[33] M.S. Islam, D.J. Driscoll, C.A.J. Fisher, P.R. Slater, Chem. Mater. 17 (2005) 5085.
[34] H. Huang, S.C. Yin, L.F. Nazar, Electrochem. Solid-State Lett. 4 (2001) A170.
[35] N. Ravet, S, Besner, M. Simoneau, A. Vallee, M. Armand, J.F. Magnan, European Patent 1049182A2 (2000); to Hydro-Quebec.
[36] R. Dominko, M. Bele, M. Gaberscek, M. Remskar, D. Hanzel, S. Pejovnik, J. Jamnik, J. Electrochem. Soc. 152 (2005) A607.
[37] M.S. Whittingham, Chem. Rev. 104 (2004) 4271.